




Structural, magnetic, dielectric and hyperfine interaction studies of titanium (Ti⁴⁺)-substituted nickel ferrite (Ni_{1+x}Ti_xFe_{2–2x}O₄) nanoparticles

B. A. Patil^{1*} , Jitendra S. Kounsalye², Ashok V. Humbe², and R. D. Kokate³

¹Department of Instrumentation, Jawaharlal Nehru Engineering College, Aurangabad, MS, India

²Department of Physics, Dr. Babasaheb Ambedkar, Marathwada University, Aurangabad, MS, India

³Department of Instrumentation, Government Engineering College, Jalgaon, MS, India

Received: 25 October 2020

Accepted: 24 December 2020

Published online:
20 January 2021

© The Author(s), under
exclusive licence to Springer
Science+Business Media, LLC
part of Springer Nature 2021

ABSTRACT

Tetravalent titanium (Ti⁴⁺)-substituted nickel ferrite nanoparticles with varying composition were prepared by standard sol–gel auto-combustion method. The phase identification and nanocrystalline nature were studied through X-ray diffraction (XRD) technique. The room temperature X-ray diffraction pattern show only those planes which belong to cubic spinel structure. No extra peak other than cubic spinel structure appeared in the XRD pattern suggesting that the prepared nanoparticles possess single-phase cubic spinel structure except $x = 0.4, 0.5$ and 0.6 . The plane (311) observed in the XRD pattern showed maximum intensity and is used to calculate the crystallite size (t). The Debye–Scherrer’s formula was used to calculate the crystallite size which was found to vary between 19 and 23 nm for varying Ti composition x . The lattice constant (a) and other structural parameters were obtained from XRD data. The lattice constant is found to be decreasing with increase in Ti substitution. The FE-SEM images of typical samples confirmed the spherical shape morphology. The magnetic properties were studied by means of vibrating sample magnetometer and Mossbauer spectroscopy technique. All the samples exhibit a good magnetic property which decreases with Ti substitution. The saturation magnetization goes on decreasing from 43.14 (for $x = 0.0$) to 12.86 (for $x = 0.5$) which may be attributed to the decreasing A–B interaction. The Mossbauer spectrum of typical samples show sextet pattern. The Mossbauer parameters like isomer shift, quadrupole splitting, Line width etc. were obtained. The dielectric parameters such as dielectric constant, dielectric loss and dielectric loss tangent etc. were recorded using vector network analyzer.

Address correspondence to E-mail: dilipanand21@gmail.com

1 Introduction

Nanoscale metal oxides are of great interest due to their usability in various basic science as well as applied research areas [1–3]. The metallic elements are capable to form a diverse type of oxide compounds [4–7]. These materials may appear as different structures with an electronic structure which can possess metallic, semiconducting or insulating behaviour. In nanotechnological application, nanoscale metal oxides are mainly employed in the design and development of micro-electronic circuit, sensors, piezoelectric devices, fuel cells and coatings etc. [8–14]. Nanoscale metal oxide may possess exceptional physicochemical gesture because of their controlled size and high density [15–17]. The polycrystalline ferrites composed of metal oxide and iron oxide show excellent combined electrical and magnetic properties [18–20]. They also display low eddy current and dielectric losses along with high electrical resistivity and high saturation magnetization. These excellent properties of ferrites are useful in information storage, transformer core, antenna rod and high-frequency device applications [21–23]. According to the crystal structure, ferrites are of three types viz. spinel ferrite, rare earth garnets and hexagonal ferrites. Spinel ferrite being a soft magnetic material is largely studied by many researchers compared to other types of the ferrites. Spinel ferrites are characterized by the formula AB_2O_4 where A belongs to divalent metal ion like cobalt, nickel, zinc etc., while B belongs to iron ions (Fe^{3+}). The crystal structure for spinel ferrite is f.c.c. cubic and belongs to $Fd3m$ spacegroup. The crystal structure of spinel ferrite possesses two interstitial sites, namely, tetrahedral denoted by (A) and octahedral denoted by [B] sites in which cations are varying valence and types can accommodate according to their site preference energy [24–26]. Usually, cations of larger radii occupy tetrahedral A-site, whereas cations of smaller radii occupy octahedral B-sites. Many researchers from different laboratories are working on spinel ferrite for different applications since last eight decades [27–32].

In the last some decades, spinel ferrites were synthesized by various methods and their structural, electrical, dielectric and magnetic properties were investigated as a function of dopant, temperature and frequency [33–35]. It was reported in the literature that the properties of spinel ferrite are modified when

substituted with divalent and trivalent cations. It was also reported that for spinel ferrite the electrical and magnetic properties are improved by substituting tetravalent ions [36–38]. With the development of nanoscience and nanotechnology in the recent years, the spinel ferrites in nanocrystalline form have gained much importance due to their excellent properties which differ from properties of bulk spinel ferrites. The nanocrystalline ferrites exhibit greater chemical stability, have large surface to volume ratio and can easily be prepared with low cost and low temperature [39, 40]. On account of these remarkable properties, nanocrystalline ferrites are found useful in several applications such as sensors, catalysts, targeted drug delivery, hyperthermia, water purification etc. Due to their multifunctional properties, they are attracted by many researchers [28, 41–49].

The important electrical and magnetic properties of these nanocrystalline ferrites are dependent on a number of factors. Among these factors, the synthesis method is dominant in obtaining high-quality nanoparticles of spinel ferrite. The annealing temperature, annealing time, nature of chelating agent, pH etc. and parameters of synthesis methods also play a significant role in enhancing the properties of spinel ferrite nanoparticles [50–52]. In general, the synthesis of spinel ferrite nanoparticles can be carried out by wet chemical methods. The sol-gel auto-combustion method is one of the best wet chemical method for the synthesis of spinel ferrite nanoparticles [53]. The method is simple, cost effective and requires low temperature [36]. Also, the method produces homogeneous particles of nanosize dimensions. Many researchers follow this method to obtain nanocrystalline spinel ferrite particles [54–56].

Nickel ferrite is one of the best magnetic material that belongs to spinel ferrite family. Nickel ferrite has important characteristics such as they possesses inverse spinel structure, high electrical resistivity, low eddy current and good magnetic properties. The inverse spinel nature of nickel ferrite can be changed to normal spinel structure when we prepare nickel ferrite in nanocrystalline form. The synthesis methods and synthesis conditions strongly affect the structure of nickel ferrite. Literature survey revealed that nickel ferrite nanoparticles in pure and substituted form have been synthesized in nanocrystalline form and studied for its structural, morphological, electrical and magnetic properties by several researchers [57–60]. The Mossbauer properties were

not much reported in the literature. Therefore, in the present work, attempt is made to investigate systematically the structural, magnetic, Mossbauer and dielectric properties of titanium-substituted nickel ferrite nanoparticles using X-ray diffraction, vibrating sample magnetometer, Mossbauer spectroscopy and vector network analyzer (VNA) technique.

2 Experimental

Sol-gel auto-combustion route was employed to synthesize nanocrystalline Ti^{4+} -substituted nickel ferrite NP's having generic formula $\text{Ni}_{1+x}\text{Ti}_x\text{Fe}_{2-2x}\text{O}_4$ (where, $x = 0.00, 0.10, 0.20, 0.30, 0.40, 0.50$ and 0.60). The nickel nitrate, ferric nitrate and tetrabutyl titanate were used as oxidant materials. Citric acid was used as chelating agent/fuel. Required amount of nitrates and fuel were dissolved separately in distilled water and tetrabutyl titanate in ethanol. To dissolve tetrabutyl titanate in ethanol completely, ammonia solution was added dropwise till the pH of solution becomes 8. Further, all the solutions were mixed together and the pH was adjusted at 7 using ammonia solution. The sol-gel auto-combustion synthesis at 7 pH was considered because of the neutral concentration and that can offer better synthesis conditions for auto-combustion reaction which ultimately decides the quality of the end product. Thus, pH value in the range of ~ 7 was considered in the present case. The neutralized solution (sol) is further stirred continually on a hotplate at 80°C until it converted into viscous gel. Further, the heat was increased to 120°C , then by sudden combustion we get porous ash of the samples. The obtained ash was then ground in a pestle using mortar, to get fine powder. The powder is annealed in a muffle furnace at 750°C , to improve the purity of the samples.

The Rigaku (Miniflex-2) X-ray diffractometer was used to obtain XRD patterns in 2θ range from 20° to 80° . The magnetic hysteresis loops were recorded using vibrating sample magnetometer (VSM) at room temperature by applying a magnetic field of the order of ± 1.5 T. The Mossbauer measurements were recorded on Mossbauer spectrometer at room temperature. The velocity calibration of the spectrometer was done by natural iron foil. The fitting was carried out by software MossWin. The different dielectric parameters such as dielectric constant, dielectric loss

and dielectric loss tangent etc. were recorded by VNA.

3 Results and discussion

3.1 X-ray diffraction

The prepared nickel ferrite nanoparticles in powder form was used to study the structural properties using X-ray diffractometer (XRD). X-ray diffraction patterns of all the compositions are shown in Fig. 1. A careful observation on the XRD pattern show the Bragg's reflections (220), (311), (222), (400), (421), (422), (511), (440), (620) and (533). These reflections are found in F.C.C. cubic structure. The samples with composition $x = 0.4$, $x = 0.5$ and $x = 0.6$ show additional peak near 33° , 41° and 67° . These impurity phases belong to Pbcu and P63/mmc space group which may be due to the formation of Fe_2O_3 and TiO_2 [61, 62]. The impurity phases may be oriented due to the insolubility of the titanium ions in NF at higher concentration. The increase in number of impurity peaks as well as their quantity with increasing Ti^{4+} concentration might be occurring due to the strain induced in crystal lattice on substituting larger Ti^{4+} ions in place of smaller Fe^{3+} ions (0.645 \AA) at the [B] site [63, 64]. Thus, the solubility limit of Ti^{4+} in nickel ferrite is up to $x = 0.3$ and these XRD patterns well match with the JCPDS card (#22-1086). All the peaks in the XRD pattern are intense and slightly broader indicating the nanocrystalline nature.

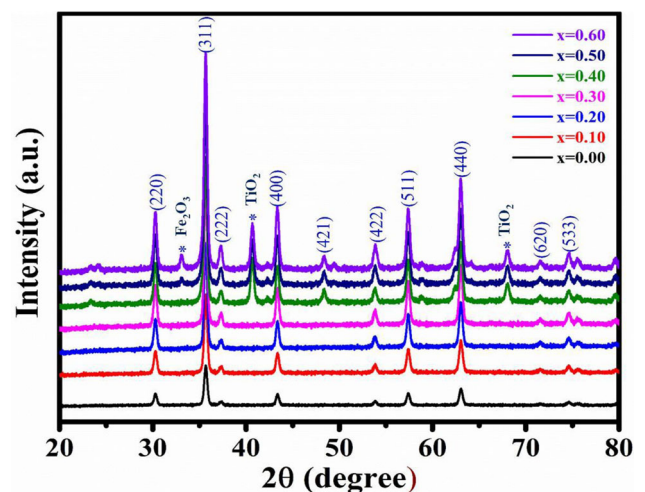


Fig. 1 X-ray diffraction pattern for $\text{Ni}_{1+x}\text{Ti}_x\text{Fe}_{2-2x}\text{O}_4$ nanoparticles

3.2 Crystallite size

The average crystallite size for each sample has been calculated using Scherrer’s formula given by

$$t = \frac{0.9\lambda}{\beta \cos\theta} \tag{1}$$

The average values of crystallite size are presented in Table 1. It is observed from Table 1 that crystallite size vary in the range from 19 nm to 23 nm.

3.3 Lattice constant

The lattice constant of all the samples was calculated by the following standard relation

$$a = d\sqrt{h^2 + k^2 + l^2}, \tag{2}$$

where symbols have their usual meanings. The obtained values of lattice constant are given in Table 1. Figure 2 depicts the variation of lattice constant as a function of Ti composition x . It is seen from Fig. 2 that, as the composition x increases up to $x = 0.4$, the lattice constant goes on increasing. Beyond $x = 0.4$, the lattice constant is found to decrease. The observed non-linear behaviour of lattice constant may be due to the change in the solubility limit. The initial increase in lattice constant may be due to the difference in ionic radii of Co^{2+} - Ti^{4+} and Fe^{3+} . In the present case, 2 Fe^{3+} ions are replaced by Co^{2+} and Ti^{4+} ions. The ionic radii of Co and Ti is greater than Fe ions, an increase in lattice constant is observed [65].

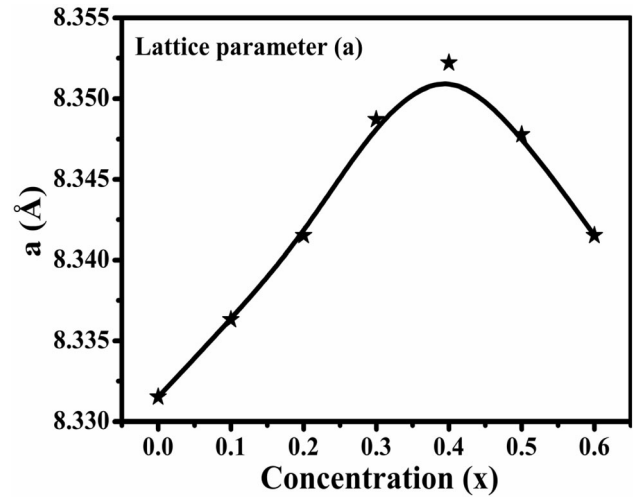


Fig. 2 Variation of lattice parameter with Ti concentration x for $\text{Ni}_{1+x}\text{Ti}_x\text{Fe}_{2-2x}\text{O}_4$ nanoparticles

3.4 Unit cell volume and X-ray density

The unit cell volume and X-ray density values obtained from the standard relations are given in Table 1. The X-ray density almost decreases with Ti composition x , whereas unit cell volume increases up to $x = 0.4$ and then decreases. The variation in the unit cell volume and X-ray density can be related to lattice constant values. It is well known that the X-ray density is indirectly dependent on the lattice constant of the materials. Thus, in the present case, the random nature of X-ray densities is attributed to the random change in the lattice constant values. Further, the values of the X-ray density are well matched with the values reported in the literature [66–69].

Table 1 Values of lattice parameter (a), X-ray density (d_x), bulk density (d_B), porosity (P %), volume (V), average crystallite size (t) and micro strain (ϵ) of $\text{Ni}_{1+x}\text{Ti}_x\text{Fe}_2\text{O}_4$

Composition ‘x’	a (Å)	d_x (g/cm ³)	d_B (g/cm ³)	P %	V (Å ³)	t (nm)	δ (lines/m ²) $\times 10^{14}$	ϵ $\times 10^{-4}$
0.00	8.3315	5.3838	3.638	32.4299	578.3	21	22.67	– 4.58
0.10	8.3363	5.2421	3.617	30.9979	579.3	20	25.02	– 3.67
0.20	8.3415	5.1001	3.587	29.6768	580.4	23	18.90	– 2.42
0.30	8.3487	4.9552	3.537	28.6244	581.9	21	22.67	– 1.26
0.40	8.3522	4.8173	3.488	27.5878	582.6	20	25.12	1.54
0.50	8.3478	4.6932	3.441	26.6770	581.7	20	25.30	2.58
0.60	8.3415	4.7038	3.441	26.8419	580.4	19	27.70	3.24

3.5 Bulk density

The bulk density was measured using Archimedes principle. The values of bulk density are also mentioned in Table 1 which clearly show decreasing trend. The bulk density of the nanoparticles depend on the synthesis method and associated parameters like type of fuel, fuel to oxidizer ratio, synthesis temperature, sintering temperature etc. The calculated values of the bulk density are matched well with that of reported in the literature [61, 70, 71]. Further, the values of X-ray density are less as compared to X-ray density.

3.6 Porosity

The percentage porosity P was also calculated using the values of X-ray density and bulk density. Table 1 gives the values of porosity in percentage. It is observed that, the percentage porosity decreases with increase in Ti^{4+} composition x . It is well known that the porosity of the nanoparticles is mainly dependent on the synthesis method and associated parameters such as type of fuel, fuel to oxidizer ration, reaction temperature, pH, sintering temperature etc. Thus, in the present case, the high values of porosity are related to the synthesis conditions. The reason for high porosity may be attributed to low temperature synthesis around 80–100 °C and due to agglomeration of the particles.

3.7 Dislocation density (δ)

The dislocation density (δ) was calculated with the help of values of crystallite size using the relation $\delta = 1/t^2$. It is well know that dislocation density indirectly depends on the crystallite size. Thus, in the present case, dislocation density showed random nature like the crystallite size values.

3.8 Micro strain (ϵ)

The values of the micro strain (ϵ) were determined by the Williamson–Hall (W–H) plot analysis as reported in the literature. The values of the micro strain (ϵ) are tabulated in the Table 1. It is observed from the table that up to $x = 0.30$ concentration it shows negative values of strain and for the further concentration it shows positive values of strain. It is well known that particles with smaller size displays – ve

slope indicating the presence of compressive strain in the material, while a + ve slope indicates tensile strain. The – ve slope of the pristine nickel ferrite shows the presence of compressive strain. It is interesting to note that the substitution of Ti^{4+} ions changes the slope values from – ve to + ve. This indicates that the substitution of Ti^{4+} ions expands the crystal lattice by altering the strain from compressive to tensile.

3.9 Hopping lengths and bond lengths

The other structural parameters like hopping lengths, interstitial radii and bond lengths were calculated using standard relations.

The hopping lengths L_A and L_B were calculated according to the following relations,

$$L_A = a\sqrt{3/4}, \quad (3)$$

$$L_B = a\sqrt{2/4}, \quad (4)$$

The tetrahedral bond length (d_{AX}), octahedral bond length (d_{BX}), tetra edge (d_{AXE}) and octa edge (d_{BXE}) were also determined for all the samples by using standard relations given below and their values are listed in Table 2.

$$d_{AX} = a\sqrt{3\left(u - \frac{1}{4}\right)}, \quad (5)$$

$$d_{BX} = a\sqrt{3u^2 - \frac{11}{4}u + \frac{43}{64}}, \quad (6)$$

$$d_{AXE} = a\sqrt{2\left(2u - \frac{1}{2}\right)}, \quad (7)$$

$$d_{BXE} = a\sqrt{2(1 - 2u)}, \quad (8)$$

$$d_{BEU} = a\sqrt{4u^2 - 3u + \frac{11}{16}}. \quad (9)$$

It is observed from Table 2 that other structural parameters such a hopping length (L_A , L_B), tetrahedral bond (d_{AX}), octahedral bond (d_{BX}), tetra edge (d_{AXE}) and octa edge (d_{BXE}) of $\text{Ni}_{1+x}\text{Ti}_x\text{Fe}_2\text{O}_4$ nanoparticles show random nature as all these values are mainly dependent on the values of lattice constant. All the values of these structural parameters are in good agreement with that reported in the literature for other spinel ferrites.

Table 2 Hopping length (L_A , L_B), tetrahedral bond (d_{AX}), octahedral bond (d_{BX}), tetra edge (d_{AXE}) and octa edge (d_{BXE}) of $Ni_{1+x}Ti_xFe_2O_4$

Composition ‘x’	L_A (Å)	L_B (Å)	d_{AX} (Å)	d_{BX} (Å)	d_{AXE} (Å)	d_{BXE} (Å) (Å)	
						Shared	Unshared
0.00	3.6077	2.9456	1.8904	2.0341	3.0870	2.8042	2.9473
0.10	2.5171	2.4376	1.8915	2.0353	3.0888	2.8059	2.9490
0.20	2.5184	2.4389	1.8927	2.0366	3.0907	2.8076	2.9509
0.30	2.5202	2.4407	1.8943	2.0383	3.0934	2.8100	2.9534
0.40	2.5211	2.4416	1.8951	2.0392	3.0947	2.8112	2.9547
0.50	2.5200	2.4405	1.8941	2.0381	3.0931	2.8097	2.9531
0.60	2.5184	2.4389	1.8927	2.0366	3.0907	2.8076	2.9509

3.10 Morphological analysis

Figure 3 shows the FE-SEM images typical samples of $Ni_{1+x}Ti_xFe_2O_4$ ($x = 0.00$ and 0.40). It is observed from the FE-SEM images that the grains are spherical in morphology and agglomerated with each other to some extent. The agglomeration observed in FE-SEM images is attributed to the interaction between magnetic nanoparticles. Also, the successful formation of nanocrystalline nature of prepared samples is confirmed through FE-SEM images. The grain size calculated from FE-SEM images is found to be 32 nm and 41 nm for $x = 0.00$ and $x = 0.40$, respectively.

3.11 Magnetic properties

Magnetic properties of all the Ti composition x were characterized by vibrating sample magnetometer (VSM) at room temperature. The magnetization (M) Vs applied field (H) plot for all the composition x is shown in Fig. 4.

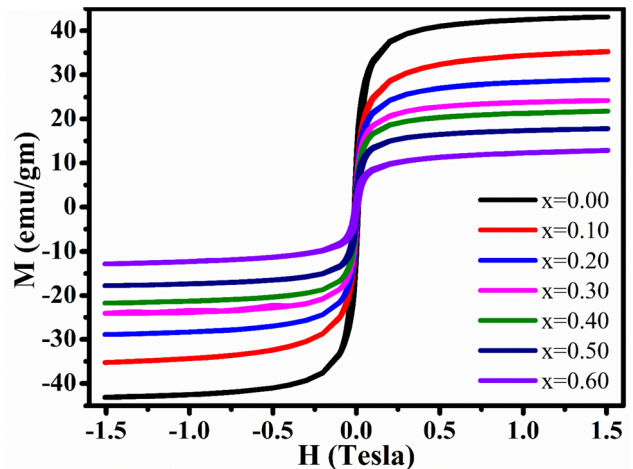


Fig. 4 $M-H$ hysteresis loop of $Ni_{1+x}Ti_xFe_{2-2x}O_4$ nanoparticles

All the samples exhibit symmetric hysteresis curve representing the superparamagnetic nature of the samples. Using these $M-H$ plots, saturation magnetization (M_S), remanence magnetization (M_r) and coercivity (H_C) were calculated and their values are summarized in Table 3.

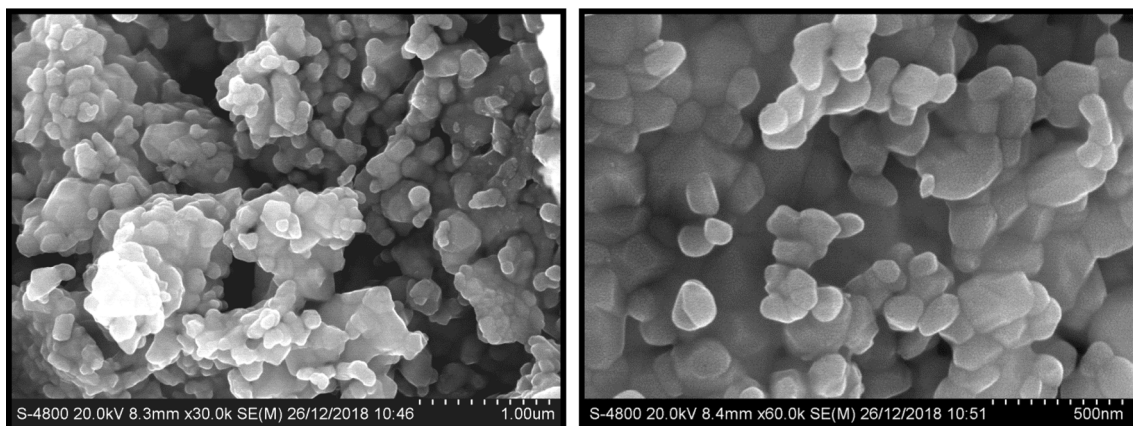


Fig. 3 FE-SEM images of typical samples of $Ni_{1+x}Ti_xFe_2O_4$ ($x = 0.00$ and 0.40)

Table 3 Saturation magnetization (M_s), remanence magnetization (M_r), coercivity (H_c), remanence ratio (M_r/M_s) and magneton number (n_B) of $Ni_{1-x}Ti_xFe_2O_4$

Composition 'x'	M_s (emu/g)	M_r (emu/g)	H_c (Oe)	M_r/M_s	n_B	K_{eff} $\times 10^{-4}$
0.00	43.142	12.569	0.013	0.29134	1.81	3.14
0.10	35.268	7.415	0.01	0.210247	1.4435	2.95
0.20	28.851	6.889	0.009	0.238779	1.1511	3.25
0.30	24.233	5.941	0.008	0.245162	0.9418	3.44
0.40	21.772	4.143	0.005	0.19029	0.8236	2.39
0.50	17.823	4.476	0.009	0.251136	0.6558	5.26
0.60	12.868	2.72	0.011	0.211377	0.4735	8.90

All these magnetic parameters decrease with increase in Ti composition x . The saturation magnetization of pristine i.e. nickel ferrite ($x = 0.0$) is in good agreement to the reported value. With substitution of non-magnetic Ti^{4+} ions, saturation magnetization decreases. In ferrite, the spin magnetic moments of both tetrahedral (A) and octahedral [B] sites are equal in magnitude, but opposite in direction, as a result they cancel each other. Within tetrahedral (A) and octahedral [B] sub-lattice, the atomic spins are parallel to each other. The resultant magnetization comes from the B-site spin moments, as B-site possesses larger magnetic moment than that of the A-site. The decrease in saturation magnetization may be attributed to lower volume fraction of ferrite phase due to decrease in super exchange interaction [72, 73]. Ti ions occupy preferentially octahedral B-site, thereby decreasing Fe^{3+} ions at octahedral B-site, which results in decrease of A–B magnetic interaction. The total number of unpaired electrons is increased at octahedral (B) site which is responsible for the enhancement of remanence.

The coercivity values are found to decrease with increase in Ti composition. Normally, the coercivity values depend on the nature of magnetic nanoparticles [74]. Single-domain nature was observed for particles with smaller size, whereas multi-domain nature was observed for particles of larger diameter [75]. For the present study, the coercivity values of all the samples are quite low representing the single-domain nature. This also suggests that, samples exhibit superparamagnetic behaviour. The remanence magnetization (M_r) also decreases with increase in Ti substitution x (Table 3). The ratio of the M_r to M_s (M_r/M_s) is the chief parameter to conclude the domain nature of the spinel ferrite materials [76]. Thus, the values of the remanence ratio (M_r/M_s) were determined from hysteresis plots. It is reported that,

if $M_r/M_s \geq 0.5$, then the materials consist of the single domain structure; however if $M_r/M_s < 0.5$, then the materials consist of the multi-domain structure. In the present case, the values of M_r/M_s vary in between 0.19 to 0.29, which is considerably less than 0.5 denoting the multi-domain structure formation in the prepared nanoparticles.

The magneton number (n_B) was also calculated using the following relation:

$$n_B = \frac{M_s \times MW}{5585}. \quad (10)$$

The values of magneton number are summarized in Table 2. It is observed that, magneton number decreases with increase in Ti composition x . The magneton number varies in accordance with the saturation magnetization. In the present study, the saturation magnetization decreases with Ti composition x and as a result magneton number also gets decreased.

The effective anisotropy constant (K_{eff}) of the samples was calculated using following equation and is listed in Table 3.

$$K_{eff} = \frac{H_c}{0.96M_s}, \quad (11)$$

where H_c is the coercivity and M_s is the saturation magnetization. The anisotropy constant is proportional to the coercivity; therefore, with a substitution, it decreases. The anisotropy of the synthesized sample mainly depends on cation distribution at [B] sites. In present investigations, non-magnetic tetravalent Ti^{4+} ions are responsible for the decrease in anisotropy with substitution.

3.12 Mossbauer properties

The Mossbauer spectra show a well-defined Zeeman pattern comprising two overlapping sextets. A

representative room temperature Mossbauer spectrum of for $x = 0.00, 0.20$ and 0.50 is shown in Fig. 5. The Mössbauer spectrum of the typical samples (Fig. 5) was fit with two Zeeman splitting patterns and one doublet. One sextet corresponding to the A-site and other sextets corresponding to the B-site Fe-atoms. The variation of line width (Γ), isomer shift (δ), quadrupole splitting (Δ), and hyperfine field (H_f) as a function of Ti^{4+} concentration is listed in Table 4. The values of line width for octahedral sites are larger than tetrahedral sites. The distribution of Ni^{2+} , Ti^{4+} and Fe^{3+} ions at (A) and [B] site is responsible for the broadening of the line width. The smaller values of isomer shift for tetrahedral sites than that of octahedral sites may be attributed to the large bond separation of $\text{Fe}^{3+}\text{-O}^{2-}$ at octahedral sites [77, 78].

The larger isomer shift at octahedral B-sites is expected owing to the overlapping of Fe^{3+} orbital ions that is small at [B] site. Moreover, the change in isomer shift with substitution was also witnessed from Table 4. The values of quadrupole splitting (Table 4) are very small, which can be attributed to the maintained cubic symmetry of Fe^{3+} and its environment. It is well known that the non-cubic symmetry arises from Fe^{2+} ions and impurity phases for 0.60 titanium concentration, which cause the large values of quadrupole splitting, while the quadrupole interaction of ^{57}Fe nuclei with electric field gradient at octahedral B-sites causes the doublet. The hyperfine magnetic field is proportional to the spontaneous magnetization of the particular sub-lattice. The hyperfine field (Table 4) consists of three components

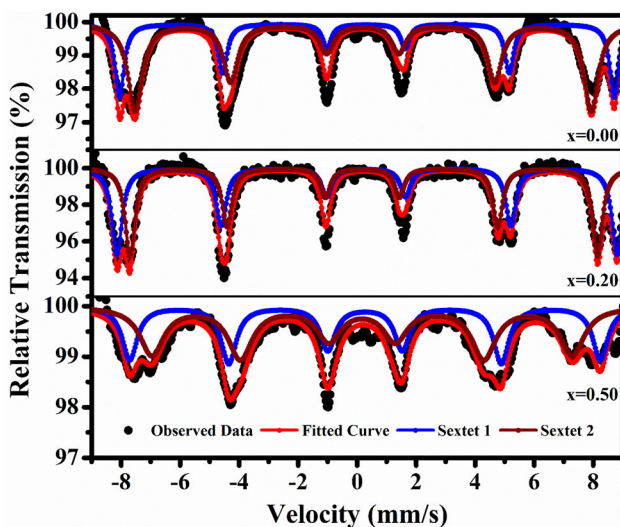


Fig. 5 Mossbauer spectra of $\text{Ni}_{1+x}\text{Ti}_x\text{Fe}_{2-2x}\text{O}_4$ nanoparticles

i.e. hyperfine field, field caused by polarization of s electrons by magnetic moments of d electrons and is the dipolar field produced by surrounding magnetic ions and H_{shift} is the super transferred hyperfine field originates from magnetic moments of nearest cations. It was observed that the hyperfine magnetic field enhanced with substitution of Ti^{4+} ions in NF.

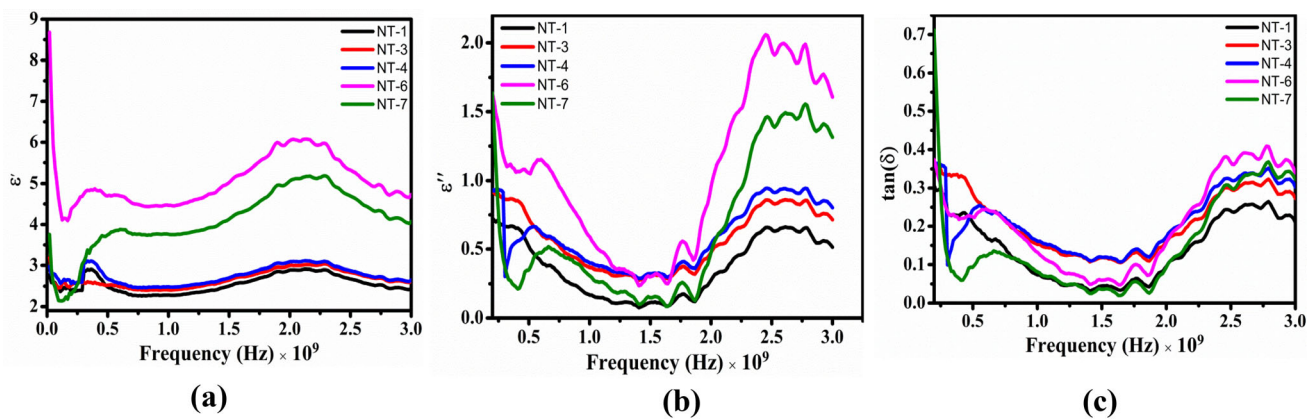
3.13 Dielectric properties

The variation of dielectric constant, dielectric loss and dielectric loss tangent etc. recorded using VNA is shown in Fig. 6a–c.

It is found that the dielectric properties were enhanced with the titanium concentration in nickel ferrite. The dielectric measurements such as real and imaginary permittivity versus frequency of titanium-substituted nickel ferrite shows that the initial permittivity increases with the increase of frequency. In X-band frequency range, all materials showed gradual increase and decrease in permittivity. Fe^{2+} ions play an important role in high-frequency permittivity of ferrite materials. The reason is that these ions have larger polarization as compared to Fe^{3+} ions. Hund's rule explained that Fe^{3+} ions have stable d-shell configuration with a spherical symmetry of charge cloud, whereas Fe^{2+} ions have an extra electron as compared to that of Fe^{3+} ions, which is distributed by the symmetry of electron cloud. Hence ferrites with a large number of Fe^{2+} ions are likely to show higher permittivity with increasing frequency. These variations were consistent with Maxwell-Wegner model and Koop's theory. The dielectric structure generally contains conducting grains, separated by a layer of grain boundaries (which formed during sintering process), which play vital role for conduction process [79, 80]. The electrons approach on these grain boundaries is due to the hopping phenomena. It is speculated that if the resistance of grain boundary is high, then the charge carriers are aligned on grain boundaries and hence polarization of dielectric materials occurs, which increases the real permittivity of materials. The dispersion process can be explained by the hopping of electrons between Fe^{3+} and Fe^{2+} ions. The exchanging of the electrons among the Fe ions i.e. $\text{Fe}^{2+} \leftrightarrow \text{Fe}^{3+}$ through oxygen is accountable for the dislodgment of electron as operated by the electric field which gives rise to polarization phenomenon in spinel ferrites [61, 81]. The small values of the grains generate larger numbers of

Table 4 Line width (Γ), isomer shift (δ), quadrupole splitting (Δ) and hyperfine field (H_f) of $\text{Li}_{0.5+0.5x}\text{Zr}_x\text{Fe}_{2.5-1.5x}\text{O}_4$ nanoparticles

Composition 'x'	Sub spectrum	Line width (mm/s)	I_S ' δ ' (mm/s)	Q. Splitting	Hyperfine field ' H_f '	(T) Area %
0.00	S1	0.36	0.31	0.03	52.11	34.38
	S2	0.55	0.19	0.01	48.04	65.62
0.20	S1	0.41	0.32	0.03	52.68	50.67
	S2	0.40	0.20	0.04	49.26	49.33
0.50	S1	0.62	0.27	0.02	49.57	42.24
	S2	0.80	0.16	0.06	44.28	57.76

**Fig. 6** Variation of **a** dielectric constant, **b** dielectric loss and **c** dielectric loss tangent for Ti-substituted nickel ferrite nanoparticles

the insulator grains boundary and thus more electron stack with the grain boundaries which raises the polarization and increases dielectric constant [82]. Charges are displaced along the direction of electric field due to electric configuration, which is responsible for polarization. This causes disorders in polarization in the material and decreases the real permittivity with the increase of frequency.

4 Conclusion

The nanoparticles of titanium-substituted nickel ferrite are successfully synthesized using sol–gel auto-combustion technique. The structural parameters are found to compatible with standard JCPDS data. All these properties are strongly affected by the impurity phases present at higher concentration of Ti in nickel ferrite; hence, it is better to bound ourselves for the substitution limit $x = 0.30$ in present system. FE-SEM images revealed the nanoscale formation and spherical shape grain morphology of the prepared nanoparticles. The saturation magnetization, coercivity and other magnetic parameters decreases with

Ti^{4+} substitution. The obtained values of magnetic parameters suggest the superparamagnetic behaviour. It is also seen from Mossbauer that the magnetization decreases rapidly after this limit. All the dielectric properties were enhanced with the titanium concentration in nickel ferrite. The structural, magnetic and dielectric properties of present investigated samples are useful for many technological and industrial applications.

Acknowledgements

One of the authors Mr. B. A. Patil is thankful to Dr. Mahaveer Singh, Department of Physics, Himachal Pradesh University, Himachal and Dr. R. S. Shinde, Raja Ramanna Centre for Advanced Technology (RRCAT), Indore for providing Mossbauer Spectroscopy facility and Dielectric measurement facility, respectively.

References

- M. Mohammadi et al., Targeted development of sustainable green catalysts for oxidation of alcohols via tungstate-decorated multifunctional amphiphilic carbon quantum dots. *ACS Appl. Mater. Interfaces*. **11**(36), 33194–33206 (2019)
- A. Ansari et al., Novel Fe₃O₄/hydroxyapatite/ β -cyclodextrin nanocomposite adsorbent: synthesis and application in heavy metal removal from aqueous solution. *Appl. Organomet. Chem.* **33**(1), e4634 (2019)
- M. Mohammadi et al., Ionic-liquid-modified carbon quantum dots as a support for the immobilization of tungstate ions (WO₄²⁻): heterogeneous nanocatalysts for the oxidation of alcohols in water. *ACS Sustain. Chem. Eng.* **7**(5), 5283–5291 (2019)
- H. Kamani et al., Sonocatalytic oxidation of reactive blue 29 by N-doped TiO₂ from aqueous solution. *J. Mazandaran Univ. Med. Sci.* **28**(166), 157–169 (2018)
- F. Moradnia et al., A novel green synthesis and characterization of tetragonal-spinel MgMn₂O₄ nanoparticles by tragacanth gel and studies of its photocatalytic activity for degradation of reactive blue 21 dye under visible light. *Mater. Res. Express* **6**(7), 075057 (2019)
- S.T. Fardood et al., Green synthesis, characterization, and photocatalytic activity of cobalt chromite spinel nanoparticles. *Mater. Res. Express* **7**(1), 015086 (2020)
- X.-W. Yan et al., Metal–organic framework derived porous 2D semiconductor C/ZnO nanocomposite with the high electrical conductivity. *Mater. Lett.* **252**, 325–328 (2019)
- V. Safarifard, A. Morsali, Facile preparation of nanocubes zinc-based metal-organic framework by an ultrasound-assisted synthesis method; precursor for the fabrication of zinc oxide octahedral nanostructures. *Ultrason. Sonochem.* **40**, 921–928 (2018)
- N.-N. Zhang et al., Ultrasonic-assisted synthesis, characterization and DNA binding studies of Ru(II) complexes with the chelating N-donor ligand and preparing of RuO₂ nanoparticles by the easy method of calcination. *J. Organomet. Chem.* **878**, 11–18 (2018)
- J.-J. Xue et al., Ultrasonic-assisted synthesis and DNA interaction studies of two new Ru complexes; RuO₂ nanoparticles preparation. *Nanomedicine* **13**(21), 2691–2708 (2018)
- P. Hayati et al., Sonochemical synthesis of two novel Pb(II) 2D metal coordination polymer complexes: new precursor for facile fabrication of lead(II) oxide/bromide micro-nanostructures. *Ultrason. Sonochem.* **42**, 310–319 (2018)
- S.M. Pormazar et al., Application of amine-functioned Fe₃O₄ nanoparticles with HPEI for effective humic acid removal from aqueous solution: modeling and optimization. *Korean J. Chem. Eng.* **37**(1), 93–104 (2020)
- T. Mortezaadeh et al., Glucosamine conjugated gadolinium (III) oxide nanoparticles as a novel targeted contrast agent for cancer diagnosis in MRI. *J. Biomed. Phys. Eng.* **10**(1), 25 (2020)
- P. Raizada et al., Silver-mediated Bi₂O₃ and graphitic carbon nitride nanocomposite as all solid state Z scheme photocatalyst for imidacloprid pesticide abatement from water. *Desalin. Water Treat.* **171**, 344–355 (2019)
- K. Atrak, A. Ramazani, S.T. Fardood, Eco-friendly synthesis of Mg_{0.5}Ni_{0.5}Al_xFe_{2-x}O₄ magnetic nanoparticles and study of their photocatalytic activity for degradation of direct blue 129 dye. *J. Photochem. Photobiol. A* **382**, 111942 (2019)
- F. Moradnia et al., Green synthesis of recyclable MgFeCrO₄ spinel nanoparticles for rapid photodegradation of direct black 122 dye. *J. Photochem. Photobiol. A* **392**, 112433 (2020)
- B.E. Azar et al., Green synthesis and characterization of ZnAl₂O₄@ ZnO nanocomposite and its environmental applications in rapid dye degradation. *Optik* **208**, 164129 (2020)
- K.K. Kefeni, T.A. Msagati, B.B. Mamba, Ferrite nanoparticles: synthesis, characterisation and applications in electronic device. *Mater. Sci. Eng. B* **215**, 37–55 (2017)
- D.S. Mathew, R.-S. Juang, An overview of the structure and magnetism of spinel ferrite nanoparticles and their synthesis in microemulsions. *Chem. Eng. J.* **129**(1–3), 51–65 (2007)
- Somvanshi, S.B., et al., Structural, thermal, spectral, optical and surface analysis of rare earth metal ion (Gd³⁺) doped mixed Zn–Mg nano-spinel ferrites. *Ceramics International*, 2020.
- A. Goldman, *Modern Ferrite Technology* (Springer, Berlin, 2006).
- A. Verma et al., Development of a new soft ferrite core for power applications. *J. Magn. Magn. Mater.* **300**(2), 500–505 (2006)
- S.R. Patade, et al., Effect of zinc doping on water-based manganese ferrite nanofluids for magnetic hyperthermia application. in *AIP Conference Proceedings*, AIP Publishing LLC, 2020
- C.R. Vestal, Z.J. Zhang, Magnetic spinel ferrite nanoparticles from microemulsions. *Int. J. Nanotechnol.* **1**(1–2), 240–263 (2004)
- T. Tatarchuk, et al., Spinel ferrite nanoparticles: synthesis, crystal structure, properties, and perspective applications, in *International Conference on Nanotechnology and Nanomaterials*, Springer, 2016
- S.B. Somvanshi et al., Hydrophobic to hydrophilic surface transformation of nano-scale zinc ferrite via oleic acid

- coating: magnetic hyperthermia study towards biomedical applications. *Ceram. Int.* **46**(6), 7642–7653 (2020)
27. H.L. Andersen et al., Crystalline and magnetic structure–property relationship in spinel ferrite nanoparticles. *Nanoscale* **10**(31), 14902–14914 (2018)
 28. K.K. Kefeni et al., Spinel ferrite nanoparticles and nanocomposites for biomedical applications and their toxicity. *Mater. Sci. Eng. C* **107**, 110314 (2020)
 29. D. Makovec et al., The synthesis of spinel–ferrite nanoparticles using precipitation in microemulsions for ferrofluid applications. *J. Magn. Magn. Mater.* **289**, 32–35 (2005)
 30. S.B. Somvanshi et al., Influential diamagnetic magnesium (Mg^{2+}) ion substitution in nano-spinel zinc ferrite ($ZnFe_2O_4$): thermal, structural, spectral, optical and physisorption analysis. *Ceram. Int.* **46**(7), 8640–8650 (2020)
 31. D. Andhare et al., Structural and chemical properties of $ZnFe_2O_4$ nanoparticles synthesised by chemical co-precipitation technique. *J. Phys.* **1644**, 012014 (2020)
 32. P.B. Kharat, S.B. Somvanshi, K. Jadhav, Multifunctional magnetic nano-platforms for advanced biomedical applications: a brief review. *J. Phys.* **1644**, 012036 (2020)
 33. M. Abdellatif, G. El-Komy, A. Azab, Magnetic characterization of rare earth doped spinel ferrite. *J. Magn. Magn. Mater.* **442**, 445–452 (2017)
 34. E.R. Kumar et al., Structural, dielectric and gas sensing behavior of Mn substituted spinel MFe_2O_4 ($M = Zn, Cu, Ni,$ and Co) ferrite nanoparticles. *J. Magn. Magn. Mater.* **398**, 281–288 (2016)
 35. V.J. Angadi et al., Structural, electrical and magnetic properties of Se^{3+} doped Mn–Zn ferrite nanoparticles. *J. Magn. Magn. Mater.* **424**, 1–11 (2017)
 36. B. Patil, R. Kokate, Synthesis and design of magnetic parameters by Ti doping in cobalt ferrite nanoparticles for nanoelectronics applications. *Proc. Manuf.* **20**, 147–153 (2018)
 37. W.W. Lukens et al., Incorporation of technetium into spinel ferrites. *Environ. Sci. Technol.* **50**(23), 13160–13168 (2016)
 38. Y. Gao et al., Electromagnetic and microwave absorption properties of Ti doped Li–Zn ferrites. *J. Alloy Compd.* **805**, 934–941 (2019)
 39. C.R. Vestal, Z.J. Zhang, Effects of surface coordination chemistry on the magnetic properties of $MnFe_2O_4$ spinel ferrite nanoparticles. *J. Am. Chem. Soc.* **125**(32), 9828–9833 (2003)
 40. K.K. Kefeni, B.B. Mamba, T.A. Msagati, Application of spinel ferrite nanoparticles in water and wastewater treatment: a review. *Sep. Purif. Technol.* **188**, 399–422 (2017)
 41. W. Hu et al., Opportunity of spinel ferrite materials in non-volatile memory device applications based on their resistive switching performances. *J. Am. Chem. Soc.* **134**(36), 14658–14661 (2012)
 42. S.R. Patade et al., Self-heating evaluation of superparamagnetic $MnFe_2O_4$ nanoparticles for magnetic fluid hyperthermia application towards cancer treatment. *Ceram. Int.* **46**(16), 25576–25583 (2020)
 43. S.B. Kale, et al. Enhancement in surface area and magnetization of $CoFe_2O_4$ nanoparticles for targeted drug delivery application, in *AIP Conference Proceedings*, AIP Publishing LLC, 2018
 44. R.M. Borade et al., Spinel zinc ferrite nanoparticles: an active nanocatalyst for microwave irradiated solvent free synthesis of chalcones. *Mater. Res. Express* **7**(1), 016116 (2020)
 45. S.R. Patade et al., Preparation and characterisations of magnetic nanofluid of zinc ferrite for hyperthermia. *Nanomater. Energy* **9**, 8–13 (2020)
 46. P.B. Kharat et al., Induction heating analysis of surface-functionalized nanoscale $CoFe_2O_4$ for magnetic fluid hyperthermia toward noninvasive cancer treatment. *ACS Omega* **5**(36), 23378–23384 (2020)
 47. S.B. Somvanshi et al., Hyperthermic evaluation of oleic acid coated nano-spinel magnesium ferrite: enhancement via hydrophobic-to-hydrophilic surface transformation. *J. Alloys Compd.* **835**, 155422 (2020)
 48. H. Kardile et al., Effect of Cd^{2+} doping on structural, morphological, optical, magnetic and wettability properties of nickel ferrite thin films. *Optik* **207**, 164462 (2020)
 49. S.B. Somvanshi et al., Investigations of structural, magnetic and induction heating properties of surface functionalized zinc ferrite nanoparticles for hyperthermia applications, in *AIP Conference Proceedings*, AIP Publishing LLC, 2019
 50. V. Sudheesh et al., Synthesis of nanocrystalline spinel ferrite (MFe_2O_4 , $M = Zn$ and Mg) by solution combustion method: influence of fuel to oxidizer ratio. *J. Alloy Compd.* **742**, 577–586 (2018)
 51. A. Salunkhe et al., Combustion synthesis of cobalt ferrite nanoparticles—influence of fuel to oxidizer ratio. *J. Alloy Compd.* **514**, 91–96 (2012)
 52. H. Waqas, A. Qureshi, Influence of pH on nanosized Mn–Zn ferrite synthesized by sol–gel auto combustion process. *J. Therm. Anal. Calorim.* **98**(2), 355–360 (2009)
 53. A. Goktas, I. Mutlu, A. Kawashi, Growth and characterization of $La_{1-x}A_xMnO_3$ ($A = Ag$ and K , $x = 0.33$) epitaxial and polycrystalline manganite thin films derived by sol–gel dip-coating technique. *Thin Solid Films* **520**(19), 6138–6144 (2012)
 54. S.A. Jadhav et al., Magneto-structural and photocatalytic behavior of mixed Ni–Zn nano-spinel ferrites: visible light-enabled active photodegradation of rhodamine B. *J. Mater. Sci.: Mater. Electron.* **31**, 11352–11365 (2020)

55. V. Bharati et al., Influence of trivalent Al–Cr co-substitution on the structural, morphological and Mössbauer properties of nickel ferrite nanoparticles. *J. Alloy Compd.* **821**, 153501 (2020)
56. A.V. Humbe et al., Cation distribution, magnetic and hyperfine interaction studies of Ni–Zn spinel ferrites: role of Jahn Teller ion (Cu^{2+}) substitution. *Mater. Adv.* **1**(4), 880–890 (2020)
57. A. Rahman et al., Fabrication of Ce^{3+} substituted nickel ferrite-reduced graphene oxide heterojunction with high photocatalytic activity under visible light irradiation. *J. Hazard. Mater.* **394**, 122593 (2020)
58. V. Manikandan et al., Fabrication of tin substituted nickel ferrite ($\text{Sn-NiFe}_2\text{O}_4$) thin film and its application as optoelectronic humidity sensor. *Sens. Actuators A* **272**, 267–273 (2018)
59. F.A. Wahaab, L.L. Adebayo, Electromagnetic properties of Cr-substituted nickel ferrite nanoparticles and their microwave absorption performance. *Ceram. Int.* **46**(18), 28506–28513 (2020)
60. V. Manikandan et al., Structural, dielectric and enhanced soft magnetic properties of lithium (Li) substituted nickel ferrite (NiFe_2O_4) nanoparticles. *J. Magn. Magn. Mater.* **465**, 634–639 (2018)
61. M. Ahmed, K. Rady, M. Shams, Enhancement of electric and magnetic properties of Mn–Zn ferrite by Ni–Ti ions substitution. *J. Alloy Compd.* **622**, 269–275 (2015)
62. A. Goktas et al., Enhancing crystalline/optical quality, and photoluminescence properties of the Na and Sn substituted ZnS thin films for optoelectronic and solar cell applications; a comparative study. *Opt. Mater.* **107**, 110073 (2020)
63. B. Ünal et al., Microwave, dielectric and magnetic properties of Mg–Ti substituted Ni–Zn ferrite nanoparticles. *Ceram. Int.* **42**(15), 17317–17331 (2016)
64. S.C. Mazumdar et al., Effect of Ti^{4+} doping on structural, electrical and magnetic properties of $\text{Ni}_{0.4}\text{Cu}_{0.2}\text{Zn}_{0.4}\text{Fe}_{2-x}\text{Ti}_x\text{O}_4$ ferrites. *Mater. Sci. Appl.* **10**(12), 733 (2019)
65. R. Rathi, R. Neogi, Structural, electric and magnetic properties of titanium doped Ni–Cu–Zn ferrite. *Mater. Today* **3**(6), 2437–2442 (2016)
66. Y. Guo et al., A facile spray pyrolysis method to prepare Ti-doped ZnFe_2O_4 for boosting photoelectrochemical water splitting. *J. Mater. Chem. A* **5**(16), 7571–7577 (2017)
67. K.P. Chae et al., Magnetic properties of Ti-doped ultrafine CoFe_2O_4 powder grown by the sol gel method. *Hyperfine Interact.* **136**(1–2), 65–72 (2001)
68. P. Chand, R.C. Srivastava, A. Upadhyay, Magnetic study of Ti-substituted NiFe_2O_4 ferrite. *J. Alloy Compd.* **460**(1–2), 108–114 (2008)
69. Y. Du et al., Valence of Ti cations and its effect on magnetic properties of spinel ferrites $\text{Ti}_x\text{M}_{1-x}\text{Fe}_2\text{O}_4$ ($\text{M} = \text{Co}, \text{Mn}$). *RSC Adv.* **8**(1), 302–310 (2018)
70. P. Hankare et al., Synthesis and characterization of nanocrystalline Ti-substituted Zn ferrite. *J. Alloy Compd.* **509**(5), 2160–2163 (2011)
71. B. Ramesh et al., Influence of Zr/Ti on dielectric behaviour of Mn–Zn ferrites. *J. Magn. Soc. Jpn.* **22**, S1_29 (1998)
72. L.-Z. Li et al., Effects of Ce substitution on the structural and electromagnetic properties of NiZn ferrite. *J. Magn. Magn. Mater.* **475**, 1–4 (2019)
73. L.-Z. Li et al., Structural and magnetic properties of Mg-substituted NiZnCo ferrite nanopowders. *Ceram. Int.* **40**(9), 13917–13921 (2014)
74. F. Önal et al., Structure and magnetization of polycrystalline $\text{La}_{0.66}\text{Ca}_{0.33}\text{MnO}_3$ and $\text{La}_{0.66}\text{Ba}_{0.33}\text{MnO}_3$ films prepared using sol-gel technique. *J. Supercond. Novel Magn.* **31**, 12 (2018)
75. Y. Köseoğlu et al., Low temperature hydrothermal synthesis and characterization of Mn doped cobalt ferrite nanoparticles. *Ceram. Int.* **38**(5), 3625–3634 (2012)
76. N. Somaiah et al., Magnetic and magnetoelastic properties of Zn-doped cobalt-ferrites— $\text{CoFe}_{2-x}\text{Zn}_x\text{O}_4$ ($x = 0, 0.1, 0.2$, and 0.3). *J. Magn. Magn. Mater.* **324**(14), 2286–2291 (2012)
77. T. Poudel et al., The effect of gadolinium substitution in inverse spinel nickel ferrite: structural, Magnetic, and Mössbauer study. *J. Alloy Compd.* **802**, 609–619 (2019)
78. I. Sharifi, H. Shokrollahi, Structural, magnetic and Mössbauer evaluation of Mn substituted Co–Zn ferrite nanoparticles synthesized by co-precipitation. *J. Magn. Magn. Mater.* **334**, 36–40 (2013)
79. S.B. Khan, S. Irfan, S.-L. Lee, Influence of Zn^{+2} doping on Ni-based nanoferrites; ($\text{Ni}_{1-x}\text{Zn}_x\text{Fe}_2\text{O}_4$). *Nanomaterials* **9**(7), 1024 (2019)
80. A. Goktas et al., Physical properties of solution processable n-type Fe and Al co-doped ZnO nanostructured thin films: role of Al doping levels and annealing. *Mater. Sci. Semicond. Process.* **75**, 221–233 (2018)
81. A. Goktas, F. Aslan, I.H. Mutlu, Annealing effect on the characteristics of $\text{La}_{0.67}\text{Sr}_{0.33}\text{MnO}_3$ polycrystalline thin films produced by the sol–gel dip-coating process. *J. Mater. Sci.* **23**(2), 605–611 (2012)
82. A.R. Chavan et al., Influence of trivalent Cr ion substitution on the physicochemical, optical, electrical, and dielectric properties of sprayed NiFe_2O_4 spinel-magnetic thin films. *RSC Adv.* **10**(42), 25143–25154 (2020)

Publisher's Note Springer Nature remains neutral with regard to jurisdictional claims in published maps and institutional affiliations.